Rare Metal Materials and Engineering
Volume 48, Issue 11, November 2019
Available online at www.rmme.ac.cn

Science Press

Cite this article as: Rare Metal Materials and Engineering, 2019, 48(11): 3476-3486.

ARTICLE

Hot Deformation Behavior of Fe-microalloyed Ti-6Al-4V Based on Experiments and Calculations

Liu Xin, Zhu Xiaoxian, Guo Yanhua, Dong Yuecheng, Dan Zhenhua, Chang Hui, Zhou Lian

Nanjing Tech University, Nanjing 210009, China

Abstract: Hot deformation behaviors of Ti-6Al-4V-0.35Fe were studied, which is significant to improve plastic deformation ability of titanium alloys. In experiment, we used a Gleeble 3800 thermo-mechanical simulator to obtain the relationship between thermomechanical parameters and flow stress in a range of temperatures (800~950 °C) and strain rates (0.001~10 s^{-1}). The single-peak profiles of the flow curves indicate that dynamic recrystallization (DRX) mechanism dominates the deformation. TEM analysis indicates that the grain size in DRX changes under different deformation temperatures, and finer grains are formed at relatively lower temperature due to the dynamic globularization. The dislocation walls are formed in subgrain boundaries due to dislocation slipping-climbing. The Avrami-type DRX model and the strain compensated multivariable regression model were applied to fit the experimental stress-strain data during hot deformation. A comparative study between these two types of constitutive models was conducted to represent the flow behavior. It is found that both models have good accuracy in predicting the flow stress of Ti-6Al-4V-0.35Fe alloy. A processing map based on dynamic material model (DMM) at the strain of 0.8 (steady-state flow stage) was established to identify the flow instability regions and stability regions. The strain rate range of stability region is 0.001~0.6 s^{-1} which has been expanded compared to the range of 0.0003~0.1 s^{-1} of Ti-6Al-4V. Optimal hot working parameters are confirmed to be 920~950 °C and 0.001~0.005 s^{-1}, and nearly complete DRX has taken place. Our results indicate that hot working property of Fe-microalloyed Ti-6Al-4V is better than that of Ti-6Al-4V alloy in 800~950 °C temperature scale, and processing cost is decreased.

Key words: titanium alloy; hot deformation; constitutive models; processing map

Due to its light weight, high strength and fracture toughness, Ti-6Al-4V(TC4) titanium alloys have been critical materials for aerospace and ocean engineering equipment. However, high deformation resistance and the high cost of hot processing of Ti-6Al-4V severely restrict their wide applications. The key to improve the hot working technology of titanium alloys is to reduce the flow stress of hot processing, which could reduce deformation resistance under the constant processing condition. Therefore, energy dissipation and hot working cost would be reduced. On the other hand, our previous work have shown that comprehensive mechanical properties of titanium alloys can be improved by the micro-addition of Fe[1,2]. Therefore, it is important to investigate flow behavior of Fe-microalloyed Ti-6Al-4V. The flow behavior of titanium alloy is always very complicated due to the fact that its hot deformation process is sensitive to many parameters such as strain capacity, strain rate and deformation temperature[3]. It is essential to obtain stress-strain curves during hot deformation and eventually to find out the optimum working condition for guiding the practical manufacturing process[4-6].

Generally speaking, the models which have been established to predict the flow stress under different deformation conditions can be classified into three categories, including physical-based constitutive model (PBC model), phenomenological constitutive model (PLC model) and artificial

Received date: November 10, 2018
Foundation item: International S&T Cooperation Program of China (2015DFA51430); National Natural Science Foundation of China (11647162)
Corresponding author: Guo Yanhua, Ph. D., College of Materials Science and Engineering, Nanjing Tech University, Nanjing 210009, P. R. China, Tel: 0086-25-83587270, E-mail: guoyanhua@njtech.edu.cn

neural network (ANN)[7]. As an effective computational approach to solve the non-linear problems, ANN can describe the flow behaviors of titanium alloy[8,9]. As a model based on empirical mathematical equations, PLC model has less material constants to be determined than PBC model[10,11]. Dynamic recrystallization (DRX) takes place during hot deformation and plays an important role in work hardening and flow softening. As a significant softening mechanism, DRX can refine the original grains effectively and achieve good high-temperature mechanical properties[12,13]. Currently, the Avrami equation has been successfully used to describe the DRX behavior[14,15]. Cai[16] predicted DRX volume fraction of AZ41M magnesium alloy through Avrami-type DRX kinetic model which has good correlation with the experimental results. Zhang[17] investigated the hot deformation behaviors of medium carbon Cr-Ni-Mo alloyed steel and adopted the kinetics models of Avrami relationship to predict the flow stress in DRX period successfully. However, due to the complexity of hot deformation behaviors and microstructural evolution of two-phase titanium alloy, limited researches considering DRX have been attempted to describe the flow behavior[11]. Consequently, it is essential to model the flow stress of Ti-6Al-4V-0.35Fe alloy in terms of the Avrami-type DRX model. The Arrhenius equation, the most widely used constitutive model, has been applied to represent the relationship between strain rate, deformation temperature and flow stress in titanium alloys[18]. In order to predict the flow curves, the method of compensation of strain is constantly proposed to obtain an accurate modified Arrhenius-type equation[8,19]. However, the calculation of activation energy in Arrhenius-type constitutive model makes it so tedious to redefine relevant parameters when the experimental data is changed. Consequently, some simple and effective PLC models would be better for predicting flow stress[9,20].

Moreover, the processing map based on dynamic material model (DMM) is an effective tool to predict the applicable hot working conditions and lessen the thermal processing defects. It is associated with the DRX, globularization of lamella and superplastic deformation in stable domains, or the flow localization, adiabatic shear bands and microscopic cracks in instable domains[21, 22]. Liu[23] had proposed the means of finite element simulation and 3-D processing maps to analyze the workability of Mg-3Al-1Zn. Zhang[24] investigated the appropriate hot working domain of lamellar Ti-43Al-2Si alloy by processing map and microstructural observation. Meanwhile, optimal thermo-mechanical parameters can be acquired from the respective processing map.

In the present study, the flow behavior analysis and the microstructural evolution of Fe-microalloyed Ti-6Al-4V were carried out to understand the characterization of hot deformation behaviors. A physically based Avrami-type DRX model and a phenomenological multivariable regression model have been proposed to investigate the hot compressive deformation behaviors. A comparative study on these two types of models is to be made to predict the flow stress under a wide range of deformation conditions. Furthermore, the optimal hot working process is to be found out by integration of the processing map and microstructure observations.

1 Experiment

Differential thermal analyses (DSC: NETZSCH, STA449) and metallographic microstructure analyses were used to measure β transus temperature. Cylindrical specimens for hot compression tests are 8.0 mm in diameter and 12.0 mm in height. The isothermal compression experiments were carried out on a Gleeble 3800 thermal-mechanical simulator at deformation temperatures of 800, 850, 900 and 950 °C , and with strain rates of 0.001, 0.01, 0.1, 1 and 10 s^{-1}. All specimens prior to deformation were heated up to the corresponding deformation temperature at a heating rate of 10 °C/s and held for 5 min in order to eliminate the effect of local temperature difference. When the deformed specimens were pressed to height reduction of 60%, the specimens were immediately quenched in water to retain the deformed microstructure.

Compressed samples were sectioned parallel to the compressing axis, and prepared through mechanical polishing and chemical etching in the Kroll's reagent. Microstructure observations were conducted by an optical microscopy (OM: ZEISS, A1M), a scanning electron microscopy (SEM) and a transmission electron microscopy (TEM, JEM2100F). The foils for TEM were prepared by a twin-jet electrolysing polisher using 30 mL perchloric acid＋170 mL butanol＋300 mL methanol as the electrolyte.

Chemical composition of Ti-6Al-4V-0.35Fe titanium alloy employed in this investigation was 6.39 Al, 4.16 V, 0.33 Fe, 0.13 O, 0.014 C, 0.016 N, and balanced Ti, and all numbers given are weight percentage (wt%). As shown in Fig.1, widmanstatten and basket-weave microstructure coexisted in the initial state, in which lamellate α colonies with 1.5~3 μm lined up in the original coarse prior β grains. The volume fraction of β phase is about 10% and the β transus temperature is 973 °C.

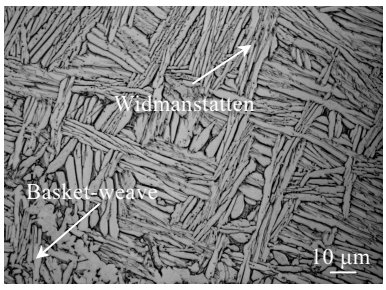

Fig.1 Initial microstructure of the Ti-6Al-4V-0.35Fe alloy before hot deformation

2 Results and Discussion

2.1 Flow behavior

Fig.2a shows the flow curves of tested titanium alloy. In the initial stage of hot deformation, work hardening causes the increase of flow stress to peak stress. With the increase of strain, the enhanced flow softening reduces flow stress gradually. Finally, because of the balance between work hardening and flow softening, the stress-strain curves of all tested alloys achieve a steady state. Compared with the values of peak stress and steady stress under different deformation conditions in Fig.2b, it is apparent that flow stress is sensitive to the deformation temperature and strain rate. At a constant strain rate, the flow stress decreases with the increase of temperature. This might be ascribed to the promotion of nucleation of DRX and improvement of grain boundary migration rate at higher temperature. Under a certain deformation temperature, the reduction of flow stress also appears with a lower strain rate which provides enough time for DRX grain to grow up[25]. This phenomenon can also be confirmed through TEM analysis in Fig.3 which shows the alloy deformed at 800 °C and a strain rate of 10^{-3} s^{-1}. Fig.3a shows that some bending subgrain boundaries occur in deformation microstructure and the dislocation walls are formed in subgrain boundaries due to dislocation slipping-climbing. When the strain rate is low enough, the dynamic recrystallized nuclei are formed which

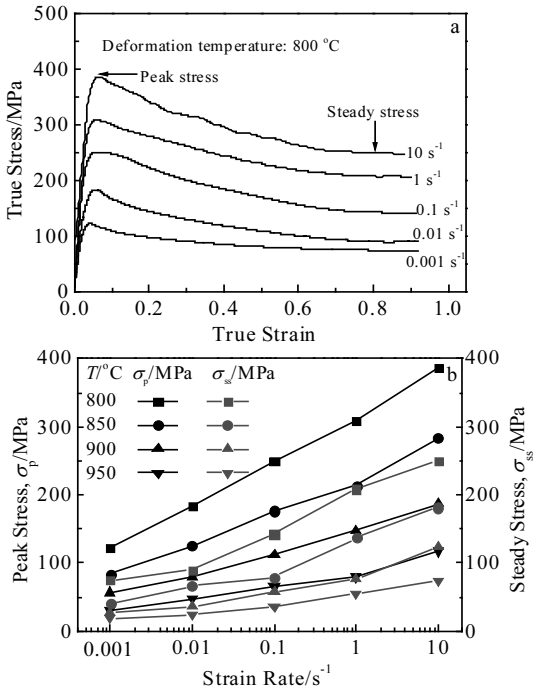

Fig.2 Typical true stress-strain curves at deformation temperature of 800 °C (a); peak stress and steady stress as functions of strain rate for different deformation temperatures (b)

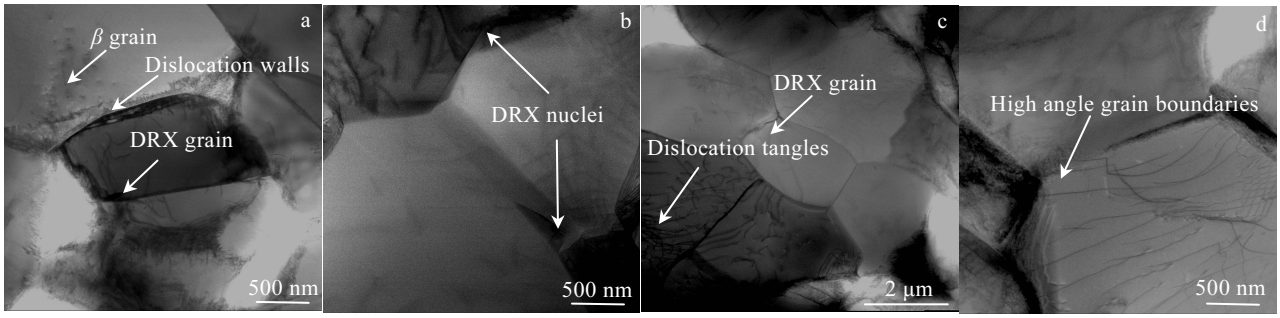

Fig.3 TEM images of specimens deformed at 800 ℃ and a strain rate of 10^{-3} s^{-1}: (a) DRX, (b) DRX nuclei, (c) dislocation tangles, and (d) high angle grain boundaries in deformed microstructure

are shown in Fig.3b. Moreover, subgrain boundaries can absorb dislocation and lead low angle grain boundaries transform into high angle grain boundaries, as shown in Fig.3d[26,27]. For the deformation of titanium alloy in the $\alpha+\beta$ dual phase region, the flow softening of lamellar microstructure usually presents DRX or dynamic globularization[28].

Fig.4a and Fig.4b indicate the occurrence of DRX in deformed samples under different deformation conditions, in which the prior β grain boundaries almost disappear and a large number of recrystallized grains are formed. As an effective method to refine the coarse β grains, DRX also can be regarded as a competitive process between nucleation and growth of recrystallized grains[3]. In the initial process of DRX, the original β grain boundaries become serrated and corrugated. Simultaneously, some fine DRX grains are formed along the β grain boundaries due to the strong driving forces for recrystallization. During the nucleation of DRX, high density dislocation would occur and develop in the nearby coarse boundaries. Subsequently, with the continuation of deformation, the conversion of dislocation cell walls leads to the formation of subgrain structure. Eventually, the dislocation completes the recovery and rearrangement, and subgrain boundaries gradually evolve into grain boundaries[29]. The growth of DRX grains

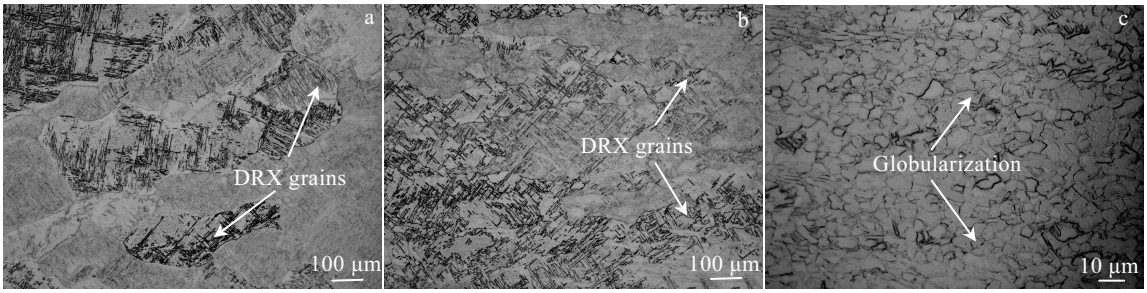

Fig.4 Microstructures of the specimens deformed under different conditions: (a) 950 °C and 0.001 s^{-1}, (b) 950 °C and 0.01 s^{-1}, and (c) 900 °C and 0.01 s^{-1}

depends on the migration of grain boundaries. The higher deformation temperature provides the driving forces for DRX, which promotes the DRX process. On the other hand, despite the lower strain rate decreases the nucleation rate of DRX grains, it supplies sufficient time for DRX grains to grow up. That is the reason that the size of DRX grains in Fig.4a is greater than that of the DRX grains in Fig.4b.

By comparing the microstructural distinction in Fig.4b and Fig.4c, it is obvious that the microstructure is inclined to present the phenomenon of dynamic globularization when the deformation temperature declines at a given strain rate. The globularization of lamellar structures at elevated temperatures, which caused by the shearing of the lamellae, was also considered to be a type of DRX[30,31].

The TEM microstructures of the studied alloy that deforms at the condition of 950 °C /10^{-3} s^{-1} are depicted in Fig.5. It is generally known to us that the slip systems in β phase is more than that in α phase in the titanium alloys, which means β phase will undergo deformation more easily. As can be seen in Fig.5a, dislocation pile-up occurs in the β phase. At the beginning stage of globularization, the imposed shear strain promotes the colonies with favorable orientations to participate in the shearing process, while the other neighbor colonies would rotate to appropriate orientations for further shear. Then the deformation induces the generation of dislocations along the line of shear. Afterwards, on intersecting slip planes, the dislocations with opposite sign would annihilate as a result of the recovery caused by cross-slip. At a higher shear strain, the original β grain boundaries become serrated (Fig.5b and Fig.5c). Meanwhile, the same sign dislocations would nucleate an interface along the line of shear. Moreover, the leaving behind dislocations with the same sign transform to substructure due to strong driving forces for recrystallization (Fig.5d). Finally, in consideration of minimizing the surface energy, the interface migration which results from diffusion effect facilitates lamellar structure to achieve globularization[31]. Based on above-mentioned analysis of microstructure, it can be concluded that the main hot deformation mechanism about flow softening in Fig.2 is DRX.

2.2 Avrami-type DRX model

The microstructure evolution of DRX primarily depends on the dislocation motion and dislocation density. When energy accumulation caused by dislocation interaction reaches to the critical value, the deformed grains begin to decompose. Meanwhile the nucleation and growth of fine DRX grains with less defects take place at fragmentized grain boundaries as well as other regions. The Avrami-type DRX model has been proved to be effective to represent the kinetics of DRX behavior. The volume fraction of DRX could be expressed as follows[17, 28]:

$$X_{\mathrm{DRX}} = 1 - \exp\left[-k\left(\frac{\varepsilon - \varepsilon_{\mathrm{c}}}{\varepsilon_{\mathrm{p}}}\right)^{N}\right] \quad (1)$$

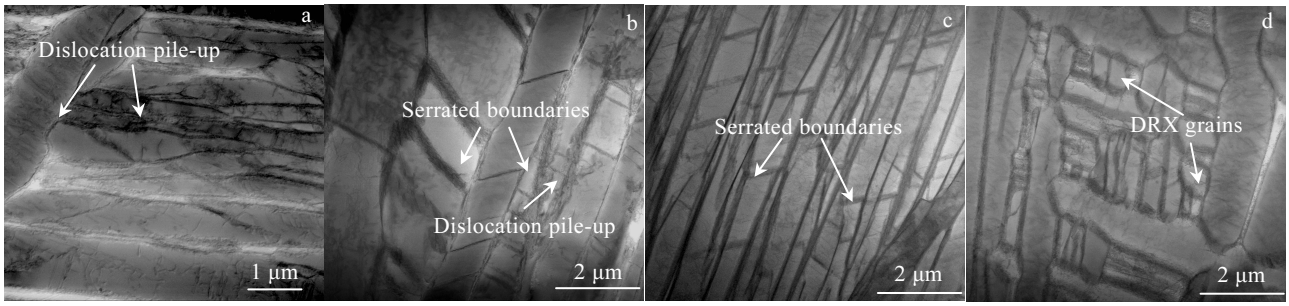

Fig.5 TEM images of specimens deformed under the condition of 950 °C/10^{-3} s^{-1}: (a) dislocation pile-up, (b) serrated boundaries and dislocation pile-up, (c) serrated boundaries, and (d) DRX

Where k and N are material constants, ε_c is the critical strain for the appearance of DRX. ε_p represents the peak strain corresponding to the peak stress.

On the other hand, the fractional softening attributed to DRX can be defined by the following equation considering net softening effect[32]:

$$X_{DRX} = \frac{\sigma_{sat} - \sigma}{\sigma_{sat} - \sigma_{ss}} \quad (2)$$

Where σ_{sat} is the saturated stress, which means the maximum stress value brought by work hardening and regardless of the effect of DRX softening. The steady-state stress, σ_{ss}, is considered as the macroscopic completion of DRX.

By combining Eqs.(1) with (2), the flow stress σ, under different degrees of DRX can be derived:

$$\sigma = \sigma_{sat} - (\sigma_{sat} - \sigma_{ss})\left\{1 - \exp\left[-k\left(\frac{\varepsilon - \varepsilon_c}{\varepsilon_p}\right)^N\right]\right\} \quad (3)$$

The application condition of Eqs.(1)~(3) is that the value of strain ε, should be no less than the critical strain ε_c, (namely $\varepsilon \geqslant \varepsilon_c$).

2.2.1 Confirmation of DRX volume fraction

The curve relation between work hardening rate (θ=dσ/dε) and flow stress is generally employed to determine the value of ε_c[33]. In this study, the stress value at the true strain of 0.8 had been adopted as σ_{ss} like the same methods in Ref.[11, 34].

Taking logarithm of both sides of Eq.(1) gives:

$$\ln\left[-\ln\left(1 - X_{DRX}\right)\right] = \ln k + N \ln\left(\frac{\varepsilon - \varepsilon_c}{\varepsilon_p}\right) \quad (4)$$

The value of k and N can be obtained from the intercept and slope of the linear relationship between ln[-ln(1-X_{DRX})] and ln[(ε–ε_c)/ε_p] (Fig.6). The values of k and N are calculated to be 0.1226 and 1.1082, respectively by means of taking average. Therefore, the DRX kinetic equation can be expressed as following:

$$X_{DRX} = 1 - \exp\left[-0.1226\left(\frac{\varepsilon - \varepsilon_c}{\varepsilon_p}\right)^{1.1082}\right] \quad (5)$$

2.2.2 Zener-Hollomon parameter

The effect of deformation temperature and strain rate on hot deformation behaviors of metallic materials could be represented by a widely used Zener-Hollomon parameter. The hot deformation behaviors can be treated as a thermally activated process like high-temperature creep. The Z parameter can be expressed with the flow stress in the following three ways[35,36]:

$$Z = \dot{\varepsilon}\exp\left(\frac{Q}{RT}\right) = \begin{cases} A_1 \exp(\beta\sigma) \\ A_2\sigma^{n_1} \\ A_3\left[\sinh(\alpha\sigma)\right]^n \end{cases} \quad (6)$$

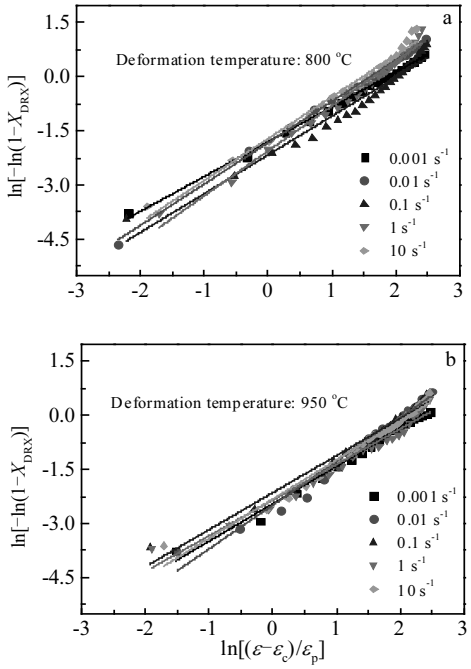

Fig.6 Linear relationships between ln[−ln(1−X_{DRX})] and ln[(ε–ε_c)/ε_p] at different deformation temperatures: (a) 800 °C and (b) 950 °C

Where $\dot{\varepsilon}$ is the strain rate (s^{-1}), Q is the deformation activation energy (kJ/mol), R is the gas constant (8.314 J/mol·K), T is the absolute temperature (K), and A_1, A_2, A_3, β, n_1, n, α ($\approx \beta/n_1$) are material constants. As the flow stress σ is dependent on the strain in Eq.(6), therefore the saturation stress or peak stress is usually applied to Eq.(6). However, saturation stress is difficult to determine precisely, and large strain at high strain rate would possibly bring about the falling of saturation stress[37]. Consequently, peak stress σ_p would be a better choose to regress the equations.

According to the power, exponential, and hyperbolic sine functions of Eq.(6), the average values of β and n_1 can be obtained from the slopes of curves of σ_p-ln$\dot{\varepsilon}$ and lnσ_p-ln$\dot{\varepsilon}$, respectively. Subsequently, in accordance with $\alpha \approx \beta/n_1$, the n value can also be determined by the linear relationship of ln[sinh($\alpha\sigma$)] and ln$\dot{\varepsilon}$. These plots are shown in Fig.7 and the value of α is calculated to be 0.007264. Simultaneously, the related mathematical expressions are as below:

$$\begin{cases} \sigma = \dfrac{1}{\beta}\ln\varepsilon + \dfrac{1}{\beta}\left(\dfrac{Q}{RT} - \ln A_1\right) \\ \ln\sigma = \dfrac{1}{n_1}\ln\varepsilon + \dfrac{1}{n_1}\left(\dfrac{Q}{RT} - \ln A_2\right) \\ \ln\left[\sinh(\alpha\sigma)\right] = \dfrac{\ln\varepsilon}{n} + \dfrac{Q}{nRT} - \dfrac{\ln A_3}{n} \end{cases} \quad (7)$$

Similarly, at a given strain rate, the value of Q can be ob-

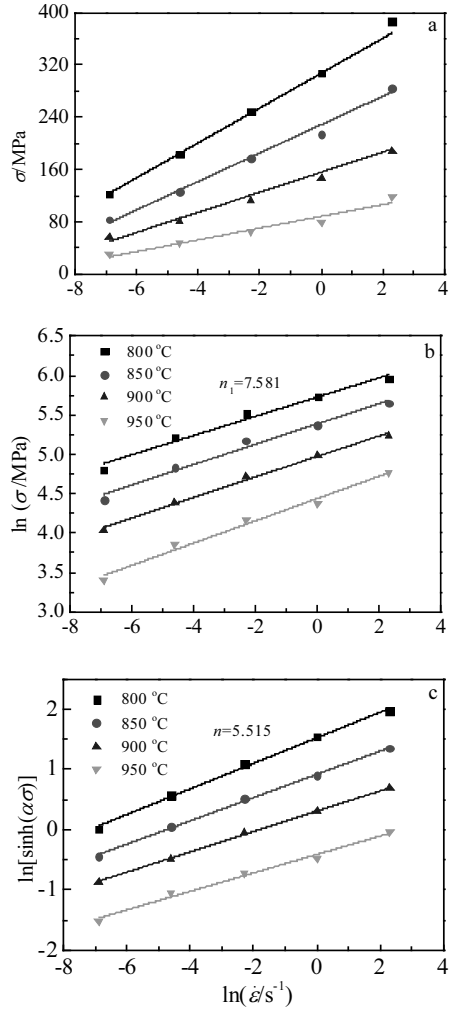

Fig.7 Relationship between σ and $\ln\dot{\varepsilon}$ (a); lnσ and $\ln\dot{\varepsilon}$ (b); ln[sinh($\alpha\sigma$)] and $\ln\dot{\varepsilon}$ (c)

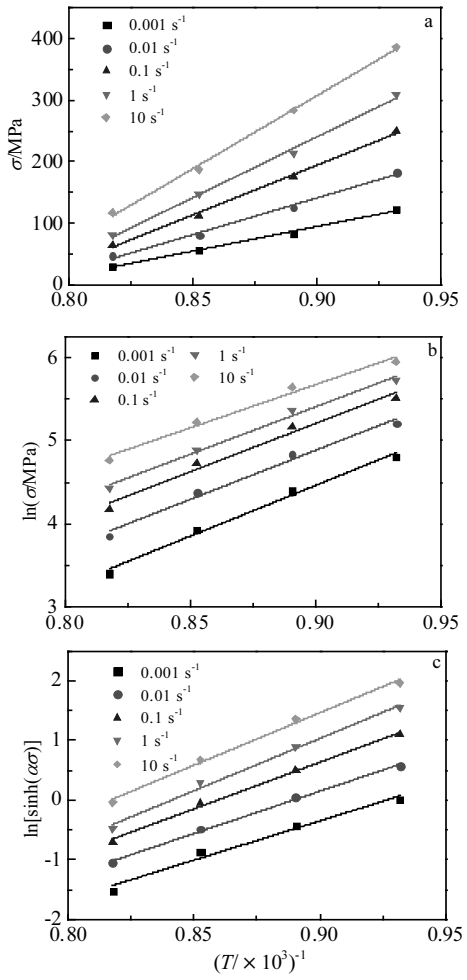

Fig.8 Linear fitting of σ(a), lnσ (b), ln[sinh($\alpha\sigma$)] (c) versus 1000/T

tained by averaging the values of Q under different strain rates as shown in Fig.8. The relevant equations are presented as following:

$$Q=\begin{cases} R\beta\left[\dfrac{\alpha\sigma}{\alpha\left(1000/T\right)}\right]_{\varepsilon} \\ Rn_1\left[\dfrac{\alpha\ln\sigma}{\alpha(1000/T)}\right]_{\varepsilon} \\ Rn\left[\dfrac{\alpha\ln\left[\sinh(\alpha\sigma)\right]}{\alpha(1000/T)}\right] \end{cases} \tag{8}$$

By comparing the activation energy Q and the adjusted R^2 error values, the values of Q under three different laws are close to each other and the hyperbolic sine law has the highest precision, relatively. Therefore, the Q value is decided to be 714.35 kJ/mol, which approaches to the value reported by Peng[19]. The mean value of lnA_3 can be derived to be 72.25 from the intercept of liner fitting of ln[sinh($\alpha\sigma$)]-ln$\dot{\varepsilon}$. Eventually, the Z parameter is obtained:

$$Z=\dot{\varepsilon}\exp\left(\frac{714350}{RT}\right)=2.3866\times10^{31}\times\left[\sinh\left(0.007264\sigma_{\mathrm{p}}\right)\right]^{5.5153} \tag{9}$$

Moreover, according to the power law equation in Eq.(5), the peak stress σ_{p} can be expressed as:

$$\sigma_{\mathrm{p}}=AZ^{B} \tag{10}$$

Jonas[32] had verified that the values of σ_{sat} and σ_{ss} have a reasonably good linear fitting relationship with σ_{p} , so σ_{sat} and σ_{ss} have the identical expression with the Z parameter. Actually, the analogous relation between ε and Z likewise had been confirmed[38]. Fig.9 shows the variation of correlation parameters in Eq.(3) with Z parameter. Then the following equations can be received in accordance with the slop and the intercept on each line:

$$\begin{cases} \sigma_{\mathrm{sat}}=0.008438\,Z^{0.1321} \\ \sigma_{\mathrm{ss}}=0.003886\,Z^{0.1348} \\ \varepsilon_{\mathrm{c}}=0.0004860\,Z^{0.05801} \\ \varepsilon_{\mathrm{p}}=0.0007878\,Z^{0.05371} \end{cases} \tag{11}$$

2.2.3 Verification of the Avrami-type DRX model

Now that the correlation parameters in Eq.(3) have been determined, hence the values of flow stress can be predicted by Eq.(3). Fig.10 presents the comparison between the experimental and calculated flow stress values. It can be seen that the predicted values are in correspondence with the experimental values except for a remarkable deviation under the condition of 800 °C/10 s^{-1}. This may be caused by the circumstance that adiabatic temperature shows a dramatic increase or the rheological instability phenomenon leads to the inapplicability of model under the lower temperature and the larger strain rate.

In order to quantify the predictability of the Avrami-type DRX model, several standard statistical parameters such as correlation coefficient (R) and average absolute relative error (AARE) have been applied. They are shown in Fig.11 and expressed as follows:

$$R=\frac{\sum_{i=1}^{N}\left(E_i-\overline{E}\right)\left(P_i-\overline{P}\right)}{\sqrt{\sum_{i=1}^{N}\left(E_i-\overline{E}\right)^2\sum_{i=1}^{N}\left(P_i-\overline{P}\right)^2}} \tag{12}$$

$$\mathrm{AARE}=\frac{1}{N}\sum_{i=1}^{N}\left|\frac{E_i-P_i}{E_i}\right|\times 100/\% \tag{13}$$

Where E_i is the experimental value of flow stress and P_i is the calculated value obtained from the model, $\overline{E}$ and $\overline{P}$ represent the mean values of all E and P, respectively. N is the total number of data employed in this study. The values of R and AARE are computed to be 0.995 and 5.15%, respectively, which reflect the good predictability of the Avrami-type DRX model.

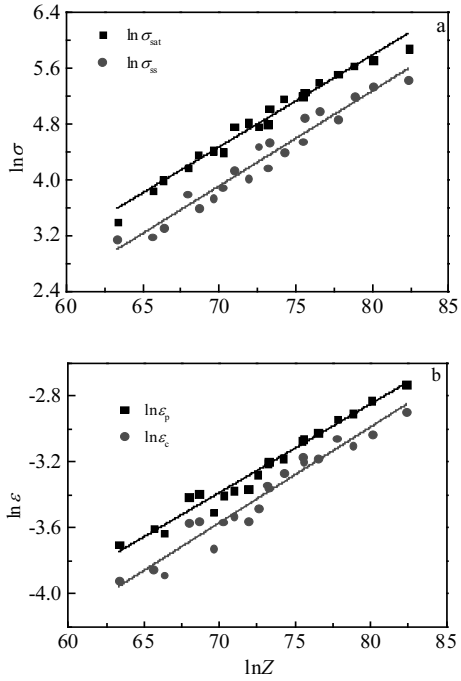

Fig.9 Relationship between $\ln\sigma$ and $\ln Z$ (a); $\ln\varepsilon$ and $\ln Z$ (b)

2.3 Multivariable regression model

It is widely known that the flow stress (σ) is significantly influenced by strain rate ($\dot{\varepsilon}$), deformation temperature (T) and strain (ε). Fig.7b and Fig.8b show that the plots of $\ln\sigma$-$\ln\dot{\varepsilon}$ at a given deformation temperature and $\ln\sigma$-1000/T under constant strain rate all have a good linear correlation. In Fig.7a and Fig.8a, linear relation of each line also presents fine but the slope of every line exhibits large disparity, which leads to the inapplicability of this multivariable regression model. Therefore, the expression about flow stress affected by strain rate and deformation temperature can be established as follows[37]:

$$\ln\sigma=M\ln\dot{\varepsilon}+N\left(\frac{1000}{T}\right)+P \tag{14}$$

Where the values of M, N and P are constants at a fixed strain.

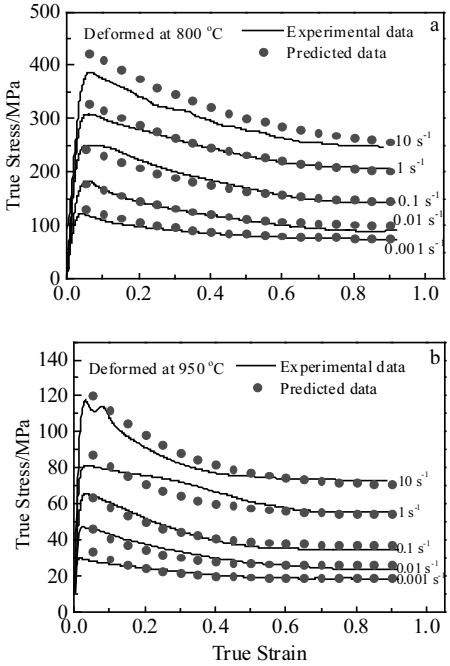

Fig.10 Comparison between the experimental and predicted flow stress by the Avrami-type DRX model at deformation temperatures of 800 °C (a) and 950 °C (b)

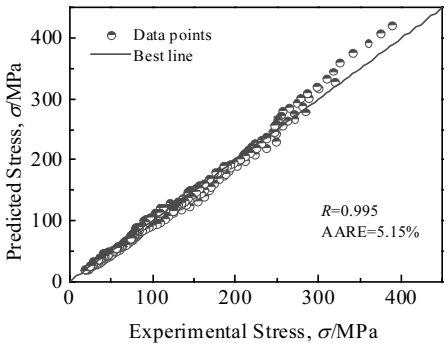

Fig.11 Correlation between the experimental and predicted flow stress by the Avrami-type DRX model for all deformation conditions by standard statistical parameters

2.3.1 Compensation of strain and the validation of model

Certainly, the effect of strain can be introduced by obtaining the development rule of parameters (*M*, *N* and *P*) at different strains. Fig.12 demonstrate the variation of *M*, *N*, *P* with taking into account the change of strain. Then the relationships of relevant parameters and strain can be fitted by a polynomial equation (the order is from 1 to 9). Among these equations, a 8th order of polynomial has been confirmed to be better due to its good correlation.

Once the correlation parameters as a function of the strain are assessed, this multivariable regression model can be used to describe the flow behavior in the temperature range of 800~950 °C and strain rate range of 0.001~10 s^{-1}. The flow stress at different deformation conditions can be calculated by Eq.(14), which is observed from Fig.13.

Fig.14 shows the correlation between the experimental and predicted flow stress data from the strain-compensated multivariable regression model, and the values of *R* and AARE are 0.995 and 4.51%, respectively. Compared to the phenomenological model represented by Arrhenius-type constitutive model, this new empirical constitutive model contains fewer variables. Compared with the Avrami-type DRX model in section 2.2, it is found that both kinds of models all possess reasonable predictability for the flow stress. Meanwhile, it is noticed that an obvious deviation also appears under the condition of 800 °C/10 s^{-1}. The actual microstructure evolution during hot deformation needs further analysis.

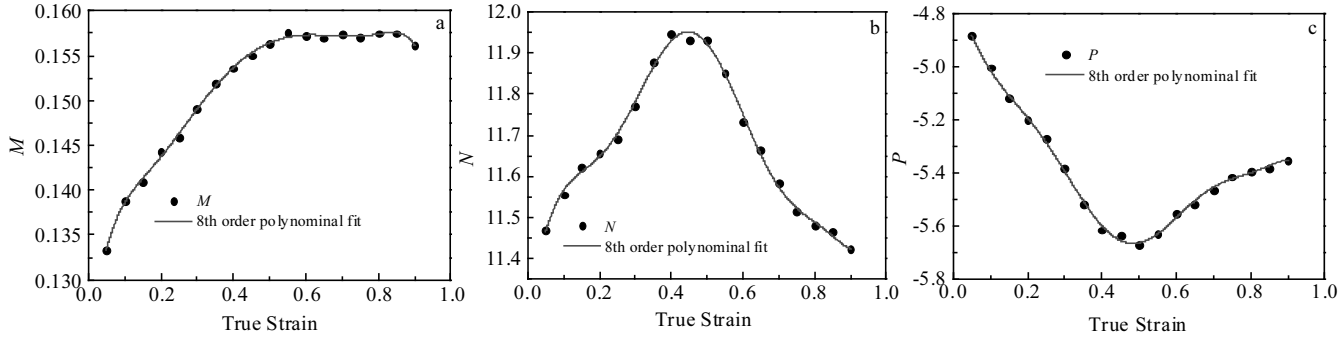

Fig.12 Polynomial fit of variation of *M* (a), *N* (b), and *P* (c) with true strain

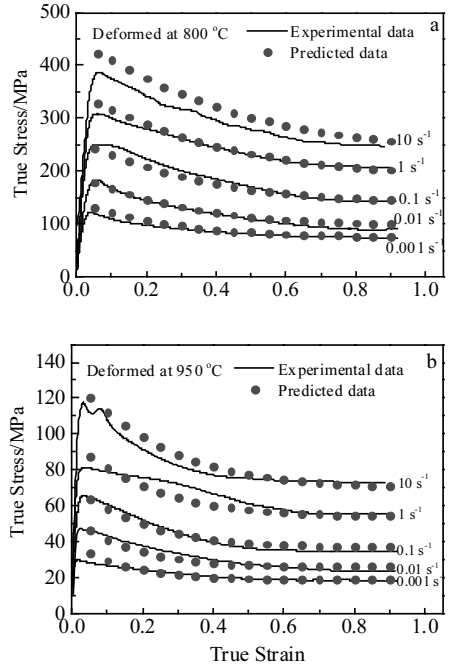

Fig.13 Comparison between the experimental and predicted flow stress by the multivariable regression model at deformation temperatures of 800 °C (a) and 950 °C (b)

2.4 Processing map of Ti-6Al-4V-0.35Fe alloy

In order to analyze the microstructural evolution and to optimize processing parameters during hot working, the processing map based on dynamic material model (DMM) is applied to model the constitutive flow behavior. In the model of DMM, the workpiece subjected to thermal deformation is considered as a non-linear dissipater of power. The absorbed energy for power dissipation can be divided into two aspects: a temperature rise generated by plastic

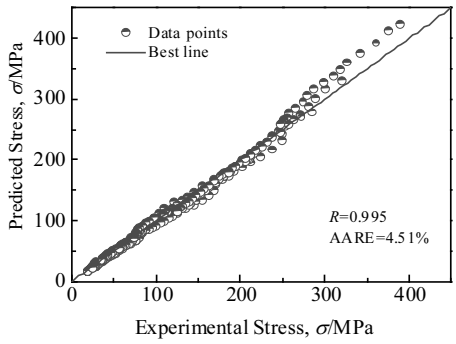

Fig.14 Correlation between the experimental and predicted flow stress by the multivariable regression model for all deformation conditions by standard statistical parameters

deformation and dissipation through microstructural change. The proportion of dissipater power content through microstructural evolution could be described by a dimensionless parameter (η), which could be expressed as[39]:

$$\eta = \frac{2m}{m+1} \tag{15}$$

Where m ($\partial \ln\sigma/\partial \ln \dot{\varepsilon}$) means sensitivity parameter of strain rate and the value of m is between 0 and 1. For an ideal linear dissipater, m reaches to the maximum.

The variation of η with temperature and strain rate establishes a power dissipation map, in which the different regions may be directly correlated with specific microstructural mechanisms. In general, the domains with higher power dissipation (η) values are beneficial to hot working. However, based on the extremum principles of irreversible thermodynamic during large plastic flow, the regime of flow instability in processing map should be determined, and the corresponding flow instability criterion is derived as[40]:

$$\xi(\dot{\varepsilon}) = \frac{\alpha \ln\left[m/(m+1)\right]}{\alpha \ln \dot{\varepsilon}} + m < 0 \tag{16}$$

Where $\xi(\dot{\varepsilon})$ is a dimensionless instability parameter. The dependence of this dimensionless parameter on deformation temperature and strain rate constitutes an instability map.

According to the steady-state flow stress values at strain of 0.8, the processing map of this Ti-6Al-4V-0.35Fe titanium alloy in the deformation temperature range from 800 to 950 °C and strain rate range from 0.001 to 10 s^{-1} is demonstrated in Fig.15. It can be found that the processing map is composed of stability domain and instability domain (the shadow region), in which the contour values indicate the efficiency of power dissipation (η). The stability domain with maximum value of η occurs in the temperature range of 920~950 °C and strain rate range of 0.001~0.005 s^{-1}. These regions with high dissipation efficiency exhibit the better hot workability. The different areas in safe regions present the varying degrees of DRX, which has been confirmed in Fig.4.

The instability domain of Ti-6Al-4V-0.35Fe alloy is in the temperature range of 800~890 °C and 910~950 °C, which correspond to the strain rate range of 0.6~10 s^{-1} and 3~10 s^{-1} respectively. Compared to that of Ti-6Al-4V-0.18Fe alloy, the instability domain shrinks, which means the extension of stability domain[2]. In addition, the maximum strain rate in stability domain is extended from 0.1 to 0.6 s^{-1} compared to that of Ti-6Al-4V[21]. And the temperature range of steady state processing is increased by 50 °C, compared to that of TC4-DT[41].

Moreover, it is worth noting that the instability domains occur in the region of strain rate above 1 s^{-1}, especially in the region with low deformation temperature. Fig.16 shows microstructure of the deformed sample at 800 °C/10 s^{-1}. It reveals the occurrence of bands of flow localization, which

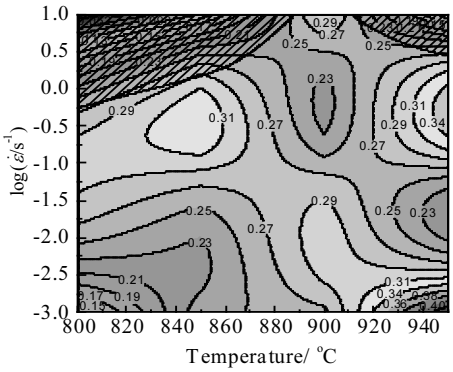

Fig.15 Processing map of tested Ti-6Al-4V-0.35Fe alloy at strain of 0.8

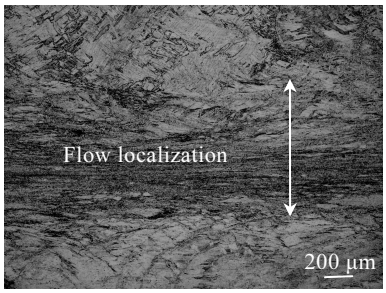

Fig.16 Flow localization of deformed sample observed at 800 °C/10 s^{-1} (white arrow stands for the direction of compression)

is nearly perpendicular to the compressive axis (the white arrow). This phenomenon is related to the increased adiabatic temperature, which is generated during the deformation. Due to the insufficient deforming time at high strain rate and the low thermal conductivity of titanium alloy material, the overmuch adiabatic deformation heat induces the formation of flow localization along the flow direction of the metal[42]. That is the reason why the evident deviation between experimental values and predicted values would appear in Fig.10a and Fig.13a.

Furthermore, in contrast to the Ti-6Al-4V alloy (containing 0.052 wt% Fe) in Ref.[45], it has been concluded that the flow stress of Ti-6Al-4V-0.35Fe alloy is lower distinctly under the same hot deformation condition. It means that deformation resistance of Ti-6Al-4V-0.35Fe alloy could be reduced in comparison of that of Ti-6Al-4V alloy under the same hot deformation condition. Therefore, a small addition of Fe element could improve the hot workability of Ti-6Al-4V effectively.

3 Conclusions

1) The typical flow curves of Ti-6Al-4V-0.35Fe alloy

express the characteristics of DRX, in which peak stress appears at low strain then followed by a gradual decline to a steady-state flow platform. Overall, the value of flow stress decreases with the increase of deformation temperature and the decrease of strain rate.

2) The Avrami-type DRX model and strain compensated multivariable regression model are used to predict the flow stress during hot compression deformation. Both models possess good prediction precision of flow behavior resulted in high R values and low AARE values.

3) According to the processing map established at strain of 0.8, the optimum hot working parameters for Ti-6Al-4V-0.35Fe alloy are obtained in the temperature range of 920~950 °C and strain rate range of 0.001~0.005 s^{-1}. The stability domain is extended with the increase of Fe content. The microstructure evolution indicates that the DRX occurs under these optimal processing conditions, while dynamic globularization occurs in the other stability domains.

References

1 Zhang Yao, Chang Hui, Li Guangzhou *et al*. *Rare Metal Materials and Engineering*[J], 2017, 46(S1):180 (in Chinese)

2 Zhu Xiaoxian, Chang Hui, Xie Yingjie *et al*. *Rare Metal Materials and Engineering*[J], 2017, 46(S1): 204 (in Chinese)

3 Peng W W, Zeng W D, Wang Q J *et al*. *Materials Science and Engineering A*[J], 2013, 571: 116

4 Liao H C, Wu Y N, Zhou K X *et al*. *Materials & Design*[J], 2015, 65: 1091

5 Ning Y Q, Fu M W, Hou H Y *et al*. *Materials Science and Engineering A*[J], 2011, 528: 1812

6 Li X, Lu S Q, Fu M W *et al*. *Journal of Materials Processing Technology*[J], 2010, 210: 370

7 Lin Y C, Chen X M. *Materials & Design*[J], 2011, 32: 1733

8 Peng W W, Zeng W D, Wang Q J *et al*. *Materials & Design*[J], 2013, 51: 95

9 Zhao J W, Ding H, Zhao W J *et al*. *Computational Materials Science*[J], 2014, 92: 47

10 Saadatkia S, Mirzadeh H, Cabrera J M. *Materials Science and Engineering A*[J], 2015, 636: 196

11 Souza P M, Beladi H, Singh R *et al*. *Materials Science and Engineering A*[J], 2015, 648: 265

12 Ning Y Q, Luo X, Liang H Q *et al*. *Materials Science and Engineering A*[J], 2015, 635: 77

13 Liu Y H, Ning Y Q, Yao Z K *et al*. *Journal of Alloys and Compounds*[J], 2016, 675: 73

14 Lv B J, Peng J, Shi D W *et al*. *Materials Science and Engineering A*[J], 2013, 560: 727

15 Bobbili R, Madhu V. *Journal of the Mechanical Behavior Biomedical Materials*[J], 2016, 59: 146

16 Cai Z W, Chen F X, Ma F J *et al*. *Journal of Alloys and Compounds*[J], 2016, 670: 55

17 Zhang C, Zhang L W, Shen W F *et al*. *Materials & Design*[J], 2016, 90: 804

18 Li C, Zhang X Y, Li Z Y *et al*. *Materials Science and Engineering A*[J], 2013, 573: 75

19 Peng X N, Guo H Z, Shi Z F *et al*. *Materials & Design*[J], 2013, 50: 198

20 Lin Y C, Liu G. *Computational Materials Science*[J], 2010, 48: 54

21 Seshacharyulu T, Medeiros S C, Frazier W G *et al*. *Materials Science and Engineering A*[J], 2000, 284: 184

22 Qu F S, Reng Z Y, Ma R R *et al*. *Journal of Alloys and Compounds*[J], 2016, 663: 552

23 Liu J, Cui Z S, Li C X. *Journal of Materials Processing Technology*[J], 2008, 205: 497

24 Zhang R, Wang D J, Liu S Q *et al*. *Journal of Alloys and Compounds*[J], 2016, 688: 542

25 Chen L, Zhang Y J, Li F *et al*. *Materials Science and Engineering A*[J], 2016, 663: 141

26 Sakai T, Belyakov A, Kaibyshev R *et al*. *Progress in Materials Science*[J], 2014, 60: 130

27 Deng Y, Yin Z M, Huang J W. *Materials Science and Engineering A*[J], 2011, 528: 1780

28 Han H F, Zeng W D, Qi Y L *et al*. *Materials Science and Engineering A*[J], 2011, 528: 8410

29 Lv B J, Peng J, Wang Y J *et al*. *Materials & Design*[J], 2014, 53: 357

30 Prasad Y V R K, Seshacharyulu T. *Materials Science and Engineering A*[J], 1998, 243: 82

31 Seshacharyulu T, Medeiros S C, Morgan J T *et al*. *Materials Science and Engineering A*[J], 2000, 279: 289

32 Jonas J J, Quelennec X, Jiang L *et al*. *Acta Materialia*[J], 2009, 57: 2748

33 Poliak E I, Jonas J J. *Acta Materialia*[J], 1996, 44: 127

34 Ma T F, Chen R R, Zheng D S *et al*. *International Journal of Hydrogen Energy*[J], 2017, 42: 8329

35 Sellars C M, Mctegart W J. *Acta Materialia*[J], 1966, 14: 1136

36 Mirzadeh H, Najafizadeh A, Moazeny M. *Metallurgical and Materials Transactions A*[J], 2009, 40: 2950

37 Azarbarmas M, Aghaie-khafri M, Cabrera J M *et al*. *Materials & Design*[J], 2016, 94: 28

38 Jorge A M, Regone W, Balancin O. *Journal of Materials Processing Technology*[J], 2003, 142: 415

39 Prasad Y V R K, Seshacharyulu T. *International Materials Reviews*[J], 1998, 43: 243

40 Chen R R, Ma T F, Guo J J *et al*. *Materials & Design*[J], 2016, 108: 259

41 Liu Jinhao, Liu Jiansheng, Xiong Yunsen *et al*. *Rare Metal Materials and Engineering*[J], 2013, 42: 1674 (in Chinese)

42 Seshacharyulu T, Medeiros S C, Frazier W G *et al*. *Materials Science and Engineering A*[J], 2002, 325: 112

基于实验与计算的 Fe 微合金化 Ti-6Al-4V 热变形行为研究

刘　鑫，朱晓弦，郭艳华，董月成，淡振华，常　辉，周　廉

（南京工业大学，江苏 南京 210009)

摘　要：对 Ti-6Al-4V-0.35Fe 合金的热变形行为进行了系统的研究。采用 Gleeble 3800 热/力模拟试验机研究了热加工参数与流变应力之间的关系，其温度范围与应变速率范围分别为 800~950 ℃与 0.001~10 s^{-1}。流变曲线的单峰分布表明, 动态再结晶机制在变形过程中占主导地位。TEM 分析表明，动态再结晶晶粒尺寸随变形温度的改变而改变，且在较低温度下由于动态球化形成了尺寸较小的晶粒。由于位错的滑移和攀移，亚晶界中形成了位错胞壁。运用 Avrami 动态再结晶模型与应力补偿多变量回归模型对热变形过程中的应力应变实验数据进行了修正。为了描述其流变行为，对这 2 种类型的本构模型进行了对比研究。实验表明，这 2 种模型对预测 Ti-6Al-4V-0.35Fe 合金的流变应力都具有良好的准确性。为了判断热加工的稳态加工区域与失稳加工区域，建立了一个应变量为 0.8，基于动态材料模型的热加工图。与 Ti-6Al-4V 钛合金相比，稳态加工的应变速率范围由 0.0003~0.1 s^{-1} 扩大到 0.001~0.6 s^{-1}。最优的热加工参数为 920~950 ℃与 0.001~0.6 s^{-1}，在此过程中几乎完全发生了动态再结晶。结果表明，在 800~950 ℃的条件下，Fe 微合金化的 Ti-6Al-4V 热加工性能优于 Ti-6Al-4V 合金，且加工成本较 Ti-6Al-4V 低。

关键词：钛合金；热变形；本构方程；加工图

作者简介：刘　鑫，男，1989 年生，硕士，南京工业大学材料科学与工程学院，江苏 南京 210009，电话：025-83587270，E-mail: liu515859@126.com